

Planar graphene-NbSe₂ Josephson junctions in a parallel magnetic field

*Tom Dvir¹, *Ayelet Zalic¹, Eirik Holm Fyhn², Morten Amundsen², Takashi Taniguchi³,
Kenji Watanabe⁴, Jacob Linder², and Hadar Steinberg¹

¹*The Racah Institute of Physics, The Hebrew University of Jerusalem, Jerusalem 91904, Israel*

²*Center for Quantum Spintronics, Department of Physics, Norwegian University of Science and Technology,
NO-7491 Trondheim, Norway*

³*International Center for Materials Nanoarchitectonics, National Institute for Materials Science, 1-1 Namiki,
Tsukuba 305-0044, Japan*

⁴*Research Center for Functional Materials, National Institute for Materials Science, 1-1 Namiki, Tsukuba
305-0044, Japan*

Abstract

Thin transition metal dichalcogenides (TMDs) sustain superconductivity at large in-plane magnetic fields due to Ising spin-orbit protection which locks their spins in an out-of-plane orientation. Here we use thin NbSe₂ as superconducting electrodes laterally coupled to graphene - making a planar, all van der Waals (vdW) two-dimensional Josephson junction (2DJJ). We map out the behavior of these novel devices with respect to temperature, gate voltage, and both out-of-plane and in-plane magnetic fields. Notably, the 2DJJs sustain supercurrent up to parallel fields as high as 8.5 T, where the Zeeman energy E_Z rivals the Thouless energy E_{Th} , a regime hitherto inaccessible in graphene. As the parallel magnetic field H_{\parallel} increases, the 2DJJ's critical current is suppressed, and in a few cases undergoes a suppression and recovery. We explore the behavior in H_{\parallel} by considering theoretically two effects: A $0-\pi$ transition induced by tuning of the Zeeman energy, and the unique effect of ripples in an atomically thin layer which create a small spatially varying perpendicular component of the field. 2DJJs have potential utility as flexible probes for two-dimensional superconductivity in a variety of materials, and introduce high H_{\parallel} as a newly accessible experimental knob.

By coupling graphene to exfoliated superconductors such as NbSe₂ [1–3] it is possible to realize Josephson junctions where both the normal and superconductor materials are two-dimensional (2D). Such junctions should sustain high in-plane magnetic fields. Thin NbSe₂ retains superconductivity at very high in-plane fields due to a combination of suppressed orbital depairing and Ising protection against pair-breaking [4, 5], and can sustain magnetic fields above 8 T without any measureable effect on the gap

*Equal contribution

size [4, 6]. Coupling graphene to two NbSe₂ flakes results in an all van-der-Waals (vdW) two dimensional Josephson junction (2DJJ). The response of such 2DJJs to in-plane magnetic field will be dictated by both spin and orbital effects. In the graphene layer, forming the weak link, the response of carrier spins to the Zeeman field may lead to interesting phenomena such as finite momentum Cooper pairing and a 0- π transition [7–10]. However, the deviation of such devices from the ideal 2D geometry due to ripples and other deformations is significant, as it gives rise to field components perpendicular to the local sample plane, introducing orbital dephasing. The latter also occurs due to the bending of magnetic field flux lines, which cannot be considered truly parallel, as they are deflected by superconducting leads [11].

2D Josephson devices are a useful platform for the study of finite momentum superconducting states: Cooper pairs may survive in the spin-polarized Fermi surface created at high magnetic fields by attaining a finite center-of-mass momentum [12, 13], which translates into a spatially varying order parameter. Finite Cooper-pair momentum $q = 2E_Z/\hbar v_F$ is dictated by the Zeeman energy $E_Z = 0.5g\mu_B H$, where g is the Landé factor, v_F is the Fermi velocity, and μ_B is the Bohr magneton. The resulting oscillation of the order parameter within the junction can create π -phase junctions, where the transition to the π -phase is found in junction lengths L determined by the multiples of π/q . Weak links characterized by large g -factors have shown signatures of finite momentum Cooper pairing [14] and allowed the realization of tunable Zeeman driven 0- π transitions [15–17]. Graphene should also exhibit a Zeeman-driven 0- π transition [7–10]. However, reaching this transition requires the application of high magnetic fields, due to the low g factor which limits the momentum shift of the Cooper pair. Ballistic graphene is uniquely expected to produce field-tunable switching between 0 and π phases while retaining a finite critical current [7], and is expected to exhibit triplet superconductivity [18].

However, the entirely 2D nature of the graphene sheet gives rise to a unique form of disorder due to graphene ripples in the third dimension. In the presence of applied H_{\parallel} this introduces a small component of perpendicular field with a disorderly spatial variation created by the ripple pattern. This effect can lead to critical current decay with parallel field, a non-Fraunhofer interference pattern, and suppression and recovery of the critical current mimicking a 0- π transition. The effect of ripples changes depending on ripple amplitude and wavelength, and junction dimensions [19]. Thus in any experiment involving graphene in parallel field, or indeed, we believe - any 2D conductor in parallel field - this effect should be considered. The morphology and effect of ripples is expected to change depending on the substrate and thickness of the 2D layer. Due to the high parallel fields sustained by the junction, our 2DJJ is sensitive to both long and short wavelength sub-milliradian curvature and sub nm height variation in graphene.

We study planar NbSe₂-Graphene-NbSe₂ junctions, fabricated by transferring cracked NbSe₂ on exfoliated graphene (see Figure 1, and detailed information in Supplementary Section 4 [20]). The thickness of the NbSe₂ flakes used for the devices in this paper was around 5-10 nm, evaluated by optical contrast. The junctions exhibit supercurrent characteristics which are similar to diffusive graphene-based devices fabricated using evaporated superconducting electrodes, including gate-tunable critical current and a Fraunhofer-like interference in out-of-plane field [21–25]. Upon application of in-plane field, the 2DJJ critical current undergoes exponential suppression and transitions from a Fraunhofer to SQUID-like interference pattern, which is retained as the field is further increased up to 8.5 T. We focus our report

on Junction A, with NbSe₂ thickness of around 10 nm and a weak link consisting of monolayer graphene. In a this device we find that the supercurrent exhibits a pronounced suppression-recovery pattern, a feature which may be associated either with a 0- π transition, or with with the effect of graphene ripples.

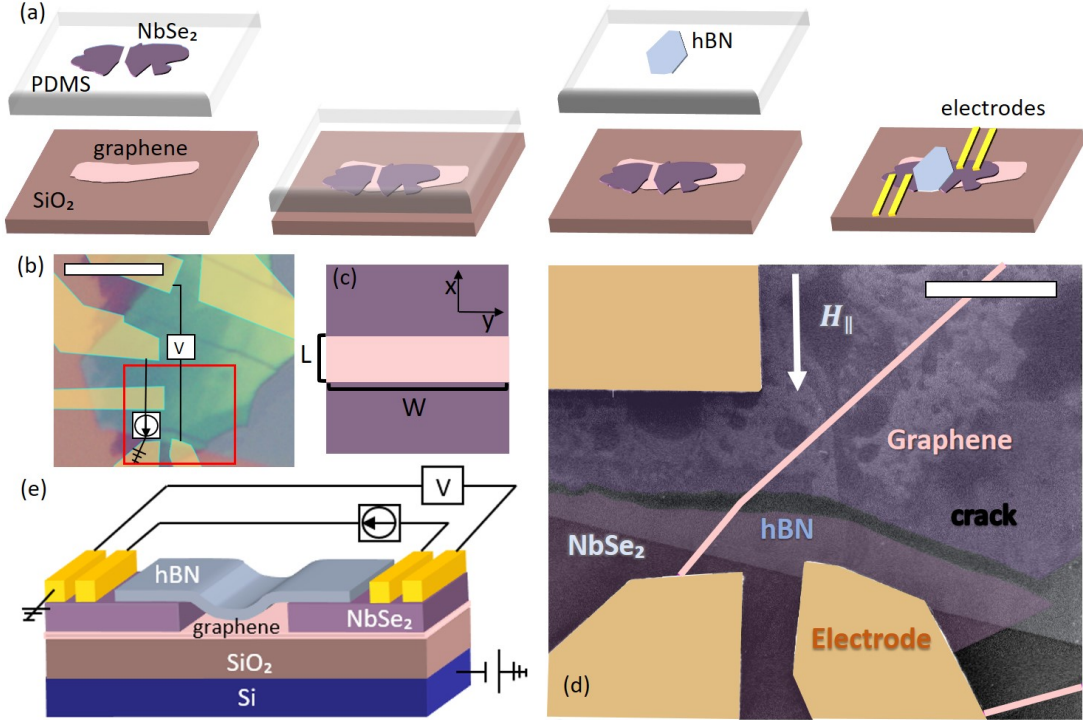


Figure 1: **a.** Fabrication of planar graphene-NbSe₂ JJs involves 1. Exfoliation of graphene on SiO₂ and NbSe₂ on PDMS. 2. Stamping a cracked NbSe₂ flake onto graphene 3. Stamping a thin hBN flake for encapsulation of the crack. 4. Patterning of electrodes. Steps illustrated from left to right **b.** Optical image of Junction A with schematics of current flow. NbSe₂ thickness is around 10 nm. Scale bar 10 μm **c.** Illustration of a rectangular junction geometry **d.** A false color SEM image of the region marked in a red square from panel b., showing the actual junction geometry, with graphene flake contour highlighted and direction of H_{\parallel} indicated. Scale bar 2 μm **e.** Schematic illustration of the JJ in a four-probe electronic configuration. Current flows in plane from NbSe₂ to graphene to NbSe₂. The crack is shielded from the top by hBN. Gate voltage is applied across the SiO₂ dielectric.

We begin by characterizing the transport of a 2DJJ. Figure 2(a) shows the typical current-voltage characteristics of Junction A, where the I - V curves at different gate voltages exhibit a switching behavior between zero resistance and finite resistance at the junction switching current I_C . Typical to density-tunable graphene JJs [21], I_C is modulated by the gate voltage V_G , and reaches a minimal, yet finite, value of $I_C \approx 0.4 \mu\text{A}$ at the Dirac point $V_G = -4$ V. This is evident in panel (b), where the differential resistance dV/dI vs. I and V_G is presented as a color plot. Thus, our 2DJJs exhibit the same bipolar super-current expected in graphene-based Josephson devices [21].

The Thouless energy, E_{Th} , defined as the inverse of the traversal time of the junction, is an energy scale characteristic of normal transport, which also governs the superconducting properties of Josephson

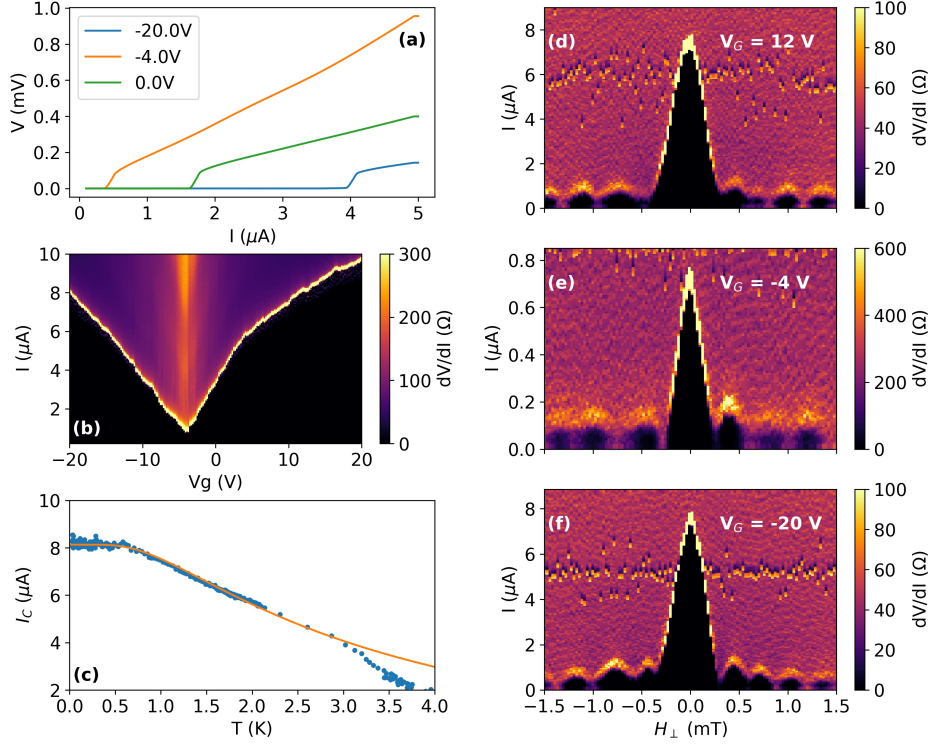


Figure 2: **a.** $I - V$ curves of Junction A (monolayer graphene) taken at different gate voltages (see legend). **b.** Differential resistance (dV/dI) of Junction A as a function of bias current and gate voltage. **c.** Temperature dependence of the critical current of Junction A (blue dots) and a fit to Eq. 1 (orange line), taken with gate voltage of -20 V. **d.,e.,f.** Differential resistance of Junction A as a function of bias current and external perpendicular magnetic field, taken with gate voltages of 12 V, -4 V (Dirac point), and -20 V, respectively. All the panels show data at $H_{\parallel} = 0$ T and $T = 30$ mK.

junctions [27]. Josephson junctions vary between regimes defined as long ($\Delta/E_{Th} \gg 1$) or short ($\Delta/E_{Th} \ll 1$), and diffusive ($L < l$) or ballistic ($L > l$), where l is the mean free path in the weak link and L is the junction length. In the diffusive case $E_{Th} = \hbar D/L^2$ where D is the diffusion constant and L is the junction length. E_{Th} and l can in principle be extracted from the dependence of graphene normal resistance on V_G [24, 25]. However, our device has an unusual geometry and non-colinear current and voltage probes, introducing uncertainties in the determination of E_{Th} . Taking l in the tens of nm, we estimate E_{Th} to be a few hundred μeV . The gap Δ of 10 nm thick NbSe₂ is close to the bulk value of 1.3 meV [28], placing Junction A in an intermediate regime, leaning towards the long and diffusive.

It is predicted that in infinitely long metallic diffusive SNS junctions, with perfect contacts, at zero temperature $eI_C R_N = \alpha E_{Th}$ (R_N is the junction normal resistance [29]). Values near the theoretically predicted value of $\alpha = 10.82$ were seen in metal SNS junctions [29], whereas in graphene α varies widely, reaching values as much as 100 times smaller than theory [22–25]. Low values of α are attributed to an

effective Thouless energy E_{Th}^* , smaller than E_{Th} determined by transport. This is possibly due to finite contact resistance and Andreev reflections across the N-S barrier which increase the time of junction traversal [25, 26]. In Junction A E_{Th} is of the order of $I_C R_N$, thus the proportionality factor α is of order unity. This indicates an effective $E_{Th}^* \approx 0.1 E_{Th}$, smaller than metallic SNS junctions and larger than previously reported diffusive graphene junctions [22–25].

In the long junction limit at low temperatures theory predicts [29]:

$$eI_C R_N = \alpha_1 E_{Th} \left[1 - b \exp \left(\frac{-\alpha_2 E_{Th}}{3.2 k_B T} \right) \right] \quad (1)$$

where $\alpha_1 = \alpha_2 = 10.82$ and $b = 1.3$. Previous attempts to fit the temperature dependence in SGS junctions led to findings of $\alpha_{1,2} = 1.1 - 2.9$ in [3, 22, 25]. In Figure 2 panel (c) we show that the temperature dependence of the critical current in Junction A fits well to an equation of this form, at low temperatures up to $T \simeq 3\text{K}$. Since we do not know the precise value of the transport E_{Th} , the fitting parameters are of limited quantitative value; nevertheless, assuming $E_{Th} \approx 300\mu\text{eV}$, We find $\alpha_1 = 1.2$, $\alpha_2 = 2.4$ and $b = 1.2$. ($\alpha_1 < \alpha_2$ was also found for similar NbSe₂ - graphene JJ's [17]). These values of $\alpha_{1,2} < 10.82$ again indicate an effective $E_{Th}^* < E_{Th}$. As we will show below, measurements at parallel magnetic fields may provide another gauge for E_{Th}^* . Next we observe the response of the system to the application of magnetic field H_\perp perpendicular to the junction plane. Figure 2 panels (d,e,f) show dV/dI as a function of H_\perp and I , taken at three different gate voltages. The observed Fraunhofer-like pattern confirms a smooth current distribution across the junction. The apparent period is 0.4 mT. We compare this to the expected period $\Phi_0/[(L+2\lambda_L)W]$, where Φ_0 is the flux quantum, L being the average junction length, and W the junction width. λ_L is the London penetration length, taken as $\lambda_L = 200\text{ nm}$ (known values in the literature range between $\approx 120\text{ nm}$ for bulk NbSe₂ [30] and 250 nm for bilayer NbSe₂ [31]). Using the above, we find the period to be $\approx 0.7\text{ mT}$ - larger than the observed period, likely due to flux focusing [11, 23]

The junction appears to retain a homogeneous current distribution even when the Fermi energy is tuned to the Dirac point - unlike ballistic graphene devices, where transport becomes dominated by edge modes [32, 33]. Close scrutiny of panels (d,e,f), however, reveals discrepancies from the perfect interference pattern: lobes are not identical, and there is an asymmetry around $H_\perp = 0$. We suggest that this asymmetry in the interference pattern is due to spatial asymmetry in junction shape and disorder potential [11, 34, 35]. Additional asymmetry could arise due to the penetration of vortices into the junction area, breaking time reversal symmetry locally [36, 37]. This will be more likely to contribute at finite H_\parallel . Having confirmed that 2DJJs have transport characteristics typical to diffusive SGS junctions [21], we turn our focus to the effect of in-plane magnetic field H_\parallel on the junction.

Since the junction is sensitive to out-of-plane fields H_\perp on the scale of a few hundreds of μT , extreme care is needed when aligning H_\perp and H_\parallel in our vector magnet to the sample geometric tilt. We do this by measuring the out-of-plane interference pattern, at any given H_\parallel . At low fields, of up to 1.5 T in Junction A, the interference pattern shows a clearly distinguishable central lobe (Fig. 3a,b), allowing for unambiguous identification of the absolute field orientation. At higher H_\parallel this is no longer possible: the central lobe is suppressed to the same magnitude of the side lobes (Fig. 3c,d). This SQUID-like

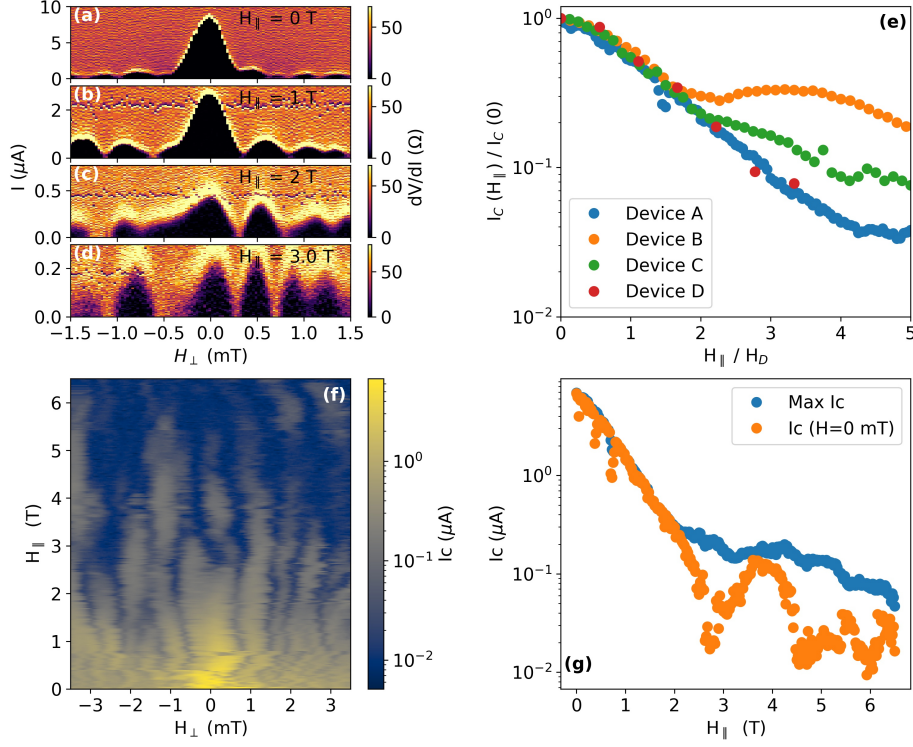


Figure 3: **a., b., c., d.** Differential resistance of Junction A as a function of bias current and external perpendicular magnetic field, taken with applied in-plane magnetic field of 0, 1 T, 2 T, and 3 T, respectively. All measurements conducted with $V_G = 20$ V. **e.** Parallel field dependence of the maximal critical current for Junctions A, B, C, D. I_C is normalized to $I_C(H_{\parallel} = 0, H_{\perp} = 0)$ and the in-plane field is normalized by a Junction-specific decay field H_D . Each value is extracted from a 2D scan of $R(V, H_{\perp})$ at a given H_{\parallel} and is defined as the maximal I_C obtained in each scan. $H_D = 0.6, 0.16, 0.4$, and 0.9 T for Junctions A,B,C,D respectively. The field at which exponential decay slows, H_T , is indicated by a dotted line for junctions A,B,C. **f.** I_C of Junction A as a function of H_{\parallel} and H_{\perp} . The curves were shifted to correct for sample misalignment, and were then aligned to be as continuous as possible. Logarithmic color-scale. **g.** Dependence of the maximal I_C (blue) and of I_C at $H_{\perp} = 0$ (orange), extracted from panel (f).

supercurrent distribution may be retained up to high parallel field. Junction A for example retains its critical current at a field of $H_{\parallel} = 8.5\text{ T}$, showing a SQUID like lobe structure as a function of H_{\perp} (Fig. 4 (a)). The voltage as a function of current curve shows a clear transition from superconducting to normal state at a critical current of $I=100\text{ nA}$ for $H_{\perp} = -2\text{ mT}$ (panel (b)).

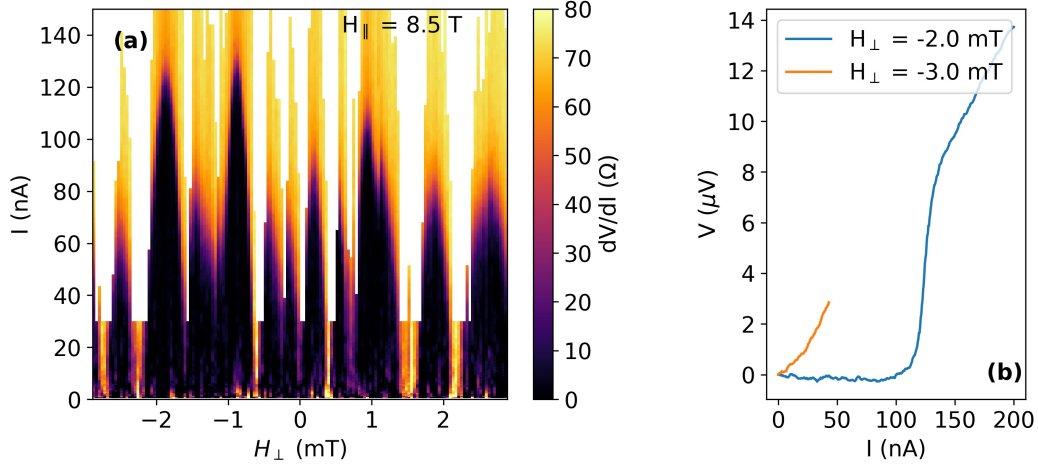


Figure 4: **High field supercurrent** (a) Interference pattern of Junction A at parallel field of 8.5 T shows clear lobes of zero resistance (data is from a different cool down than 3). (b) I-V curve from (a) where the critical current is maximal (blue) and minimal (orange). The measurement was set to stop when normal state transport is observed.

Once the central lobe is no longer distinguishable, there is in general no straightforward indication to the true position of $H_{\perp} = 0$. Lacking this identification, we take the maximal $I_C(H_{\perp})$ (hence I_C^{max}) as a measure for the junction critical current at each H_{\parallel} . We find that $I_C^{max}(H_{\parallel})$ exhibits an exponential-like decay - corresponding to the suppression of the central lobe seen in Fig 3a-c. Normalizing to $I_C^{max}(H_{\parallel} = 0)$, we plot $I_C^{max}(H_{\parallel})$ in panel (e) for Junctions A,B,C,D (all have monolayer graphene weak links, except Junction B which is bilayer graphene). To see the universality of the decay of $I_C(H_{\parallel})$, we normalize it by a junction-specific decay field, H_D . The universal decay in I_C^{max} persists up to a second characteristic field scale, H_T , where I_C^{max} stabilizes to the critical current of the side lobes. Depending on the sample, at $H > H_T$ the exponential decay in I_C^{max} either becomes moderate, or even turns into a small increase. For Junctions A,B,C shown in panel (e) this field is given by $H_T = 2.4\text{ T}$ ($4 H_D$), 0.24 T ($1.5 H_D$), and 0.8 T ($2 H_D$) respectively. In Junction D there are not enough data points to quantify this field. The junctions thus evolve to a SQUID-like lobe structure at finite, yet device-dependent H_{\parallel} (see Supplementary Section 3 [20]). The Zeeman effect in a uniform junction predicts universal decay with H_{\parallel} . Deviation from universal behavior at H_T could be a result of ripples or junction non-uniformity as we will discuss.

We now turn our attention to Fig. 3(f), which depicts the evolution of I_C vs. H_{\perp} and H_{\parallel} in Junction A. In this junction we were able to track the evolution of the interference pattern up to $H_{\parallel} = 6.5\text{ T}$, aligning the $I_C(H_{\perp})$ curves as explained in Supplementary Section 1 [20], and thus obtaining the map

shown in panel (f)¹. The magnitude of $I_C(H_{\parallel}, H_{\perp} = 0)$, plotted in panel (g), shows a suppression and recovery pattern. This data is reminiscent of suppression-recovery patterns seen in superconductor-ferromagnet-superconductor (SFS) junctions [38–43] and in 2D systems [14, 15, 17], where it is interpreted as a $0 - \pi$ transition.

The salient features of the data are therefore (a) exponential decay of the critical current at low field (b) saturation of the critical current at intermediate fields (c) lobe structure transition from Fraunhofer-like to SQUID-like, and (d) vanishing and reappearing of the central lobe critical current in Device A. In what follows, we discuss the physics in our 2DJJ by considering both the parallel field-tunable Zeeman splitting of the graphene band structure, and the orbital effect of out-of-plane ripples in the graphene [19].

Lacking an intrinsic spin-orbit coupling, graphene dispersion is affected by magnetic field only through Zeeman splitting, where the Zeeman energy is analogous to the exchange interaction in SFS JJs [19, 44]. In the latter, the superconducting order parameter in the ferromagnetic layer varies as the product of an exponential decay and an oscillatory term:

$$\psi(x) = \psi_i \exp(-k_1 x) \cos(k_2 x) \quad (2)$$

where $\psi(x)$ is the order parameter at the position x along the junction, ψ_i is the order parameter at the superconducting lead, and k_1, k_2 are the inverse characteristic length scales associated with the decay and oscillation. In the diffusive limit, they are both given by $1/k_1, 1/k_2 = \sqrt{L^2 E_{Th}/E_Z} = \sqrt{2D/g\mu_B \hbar}$ where D is the diffusion coefficient.

The order parameter thus experiences a decay accompanied by oscillation, with zeros occurring periodically when $Lk_2 = \pi/2 + n\pi$, or $E_Z = (\pi/2 + n\pi)^2 E_{Th}$. This behavior of the order parameter leads to an oscillatory decay of the critical current of the junction. Following this intuition, critical current of an SGS junction in a parallel magnetic field is thus expected to undergo an exponential suppression at low fields - in agreement with our observations. The oscillatory component of the wave function leads to a $0-\pi$ transition: a change of the equilibrium phase difference between the two superconducting leads, accompanied by a reversal of the supercurrent.

Using the analytical solution of the Usadel equations in an SGS junction [19] to qualitatively model our system, we calculate the critical current as a function of H_{\parallel} and H_{\perp} specifically for Junction A. We assume the junction length $L = 214 \text{ nm}$ and width $W = 4.69 \mu\text{m}$ (average dimensions taken from the SEM measurement shown in Fig. 1 (c)). Results are shown in Fig. 5 panel (a). The assumed uniform supercurrent reversal manifests in the suppression of all lobes, corresponding to the disappearance of the uniform supercurrent throughout the junction at a numerically determined transition field [19]:

$$H_{\parallel} \approx \frac{2.5 E_{Th}}{0.5 g \mu_B} = \frac{5 D \hbar}{g \mu_B L^2} \quad (3)$$

From the experimentally observed transition field of 2.8 T, assuming $g = 2$ we find $E_{Th} = 64 \mu\text{eV}$. This falls between the order of magnitude expected for E_{Th} of hundreds of μeV which we extract from

¹data in 3 panels (a)-(d) comes from a different measurement than panel (f), taken on the same device, and show a slightly different lobe structure

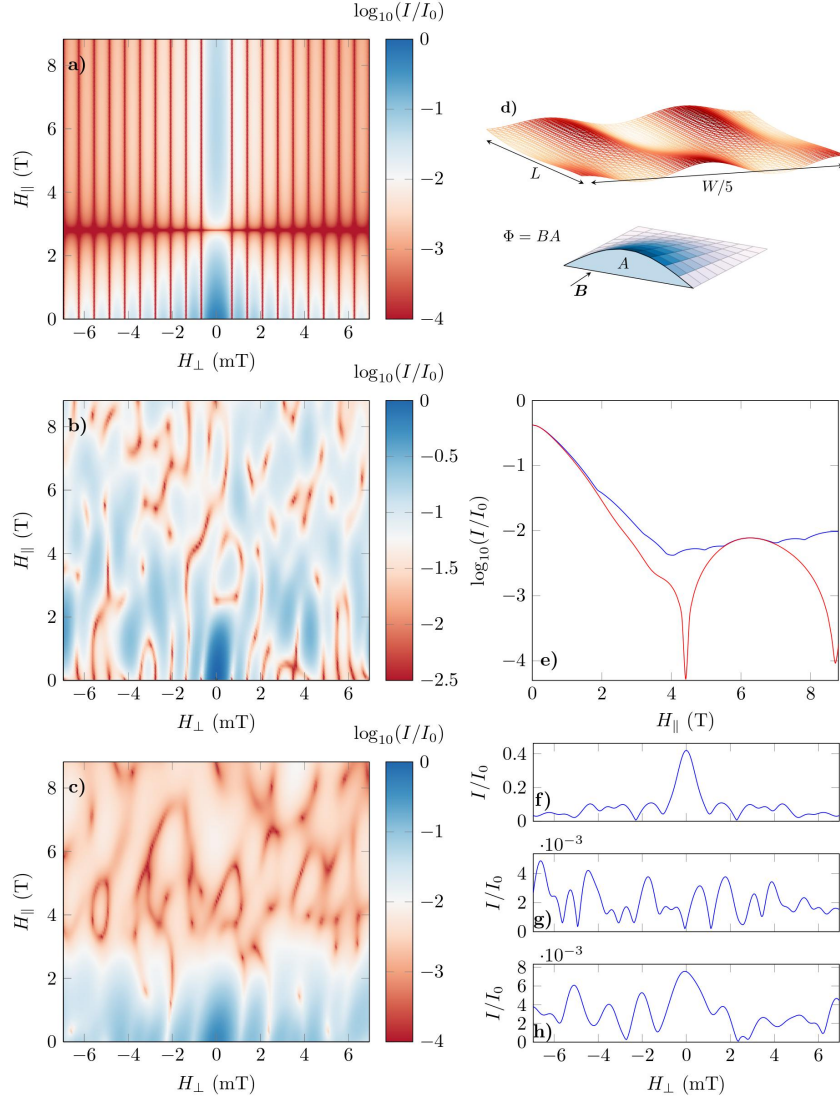


Figure 5: **a.-c.** Calculated critical current I_C with logarithmic color-scale as a function of H_\perp and H_\parallel **a.** simulated Zeeman effect with $E_{Th} = 64 \mu\text{eV}$, and a rectangular junction of dimensions $L = 214 \text{ nm}$, $W = 4.69 \mu\text{m}$ without ripples **b.** a rectangular junction with ripples, disregarding the Zeeman effect and **c.** our measured junction contour with varying L , $E_{Th} = 64 \mu\text{eV}$, Zeeman effect and ripples **d.** Top: ripple profile used to generate the maps in (b),(c). Note that the actual aspect ratio is around $W/L=20$ Bottom: illustration of a long wavelength ripple which could give rise to a zero in I_c at low fields. **e.** I_C at $H_\perp = 0$ (red) and maximal I_C for all H_\perp (blue) vs. H_\parallel , line cuts taken from the simulation in (c). **f.-h.** I_C vs. H_\perp for $H_\parallel = 0, 4.1$ and 6.2 T , line cuts from the simulation in (c)

normal regime transport properties, and E_{Th}^* of tens of μeV extracted from $I_C R_N$. Recalling that a lower effective E_{Th} has been attributed to Andreev reflection across an imperfect S-N interface, we point out that there is to the best of our knowledge no theory addressing how this would effect the Zeeman physics in the junction.

In the data in Fig. 3 (f) we find that high order lobes are retained while the zero lobe, representing the average supercurrent, is suppressed. This indicates that the supercurrent is nonuniform. When multiple transport channels are present, they may carry positive and negative supercurrents which cancel out at $H_{\parallel} = 2.8 \text{ T}$ where the central lobe vanishes. In this regime the other lobes of the interference pattern, measuring higher moments of the supercurrent with respect to the out-of-plane field, should not in general disappear. This phenomenon was seen in SFS JJs with a non-uniform ferromagnetic barrier, leading to a similar interference pattern [45–48]. Non-uniformity in supercurrent reversal can arise from local variation in E_{Th} , since regions with lower E_{Th} will undergo stronger suppression due to E_Z . Such variation in E_{Th} can arise from varying junction length, as well as from local variations in contact transparency. Additionally, it could be a consequence of charge disorder, locally affecting the diffusion constant. However, the observed SQUID-like interference pattern can only be reproduced by an E_{Th} profile which sharply favors edge transport.

We now turn to the orbital effects associated with the locally varying perpendicular components of H_{\parallel} . These variations may be caused either by graphene height variations, or by disruptions to the parallel field due to the Meissner effect, which diverts flux lines around the superconducting electrodes (flux-focusing). Because both ripples and flux-focusing give rise to a spatially varying perpendicular field component, their effect on the electric current is similar. For concreteness we give an in-depth discussion of the ripple scenario, but note that underlying mechanism could in principle also be flux-focusing.

Using the same model discussed previously, we distinguish between the effects of short and long wavelength ripples [19]. Short ripples as seen in microscopy studies of graphene on SiO_2 are typically $\approx 0.3 \text{ nm}$ peak-to-peak with a correlation length of 10-30 nm [49–52]. Long ripples have a wavelength larger than the junction dimensions. Intuitively, one may gauge the effect of a ripple by calculating the flux accumulated within an area defined by the ripple lateral cross section, illustrated in Fig. 5 (d). To induce a full current suppression and revival at $H_{\perp} = 0$, a ripple within the junction has to accumulate a single flux quantum due to the parallel field, according to the equation:

$$H_{\parallel} = \frac{\Phi_0}{\eta\lambda} \quad (4)$$

where η is the average ripple amplitude within the junction, and λ is the wavelength (or the limiting junction dimension if the ripple extends beyond the junction). For the typical short wavelength ripple seen in graphene on SiO_2 , parallel fields of order 50 T are required to obtain an entire flux quantum within a ripple. However the cumulative effect of many such ripples causes a faster decay of the critical current which can create exponential-like behavior, similar to the Zeeman effect [19].

2DJJs in a parallel field are highly sensitive to long-wavelength height variations [19]. In our experimental geometry, with junction width $W \approx 4.7 \mu\text{m}$, it is possible to consider a ripple of length $\lambda \simeq W$. As a long wavelength feature accumulates much more flux, it is possible to reach a flux quantum given a

few T parallel field and a small height variation of $\eta \approx 0.1$ nm within the junction. We note that based on AFM and STM studies, it is difficult to tell whether such sub nm height variations are present over micron length scales. Such geometry is physically conceivable due to strain or curvature of the substrate, and cannot be ruled out. We show the simulated supercurrent in a sample ripple configuration containing ripples in Fig. 5 (b). The simulation reproduces the features of the data highlighted previously - exponential decay followed by saturation, lobe structure transition, and a critical current dip at around $B = 3$ T. The specifics of these features, such as the location and sharpness of the critical current dip, vary with different ripple configurations, however many different patterns can produce qualitatively similar results (see Supplementary Section 2 [20]). Fig. 5 (d) illustrates the specific ripple profile used to obtain the map in (b). The simulation does not include ripples of wavelength smaller than around 100 nm. These in general cause a sharper decay of critical current with parallel field [19].

Since we expect Zeeman and ripple effects to coexist, we present a compound simulation which considers them both (Fig. 5 (c)). This simulation also accounts for varying E_{Th} due to variation in junction length as extracted from the SEM data presented in Fig. 1 (c). In the case of varying junction length our analytical model is not rigorous, but it does give a qualitative approximation. As we see in panel (e), the simulation reproduces the exponential decay, suppression and recovery of $I_C(H_{\parallel}, H_{\perp} = 0)$. The lobe structure at $H_{\parallel} = 0, 4.1, 6.2$ T (panels (f)-(h)), exhibits the experimentally observed transition between Fraunhofer-like and SQUID-like profiles.

Finally, we observe how the application of H_{\parallel} affects the gate dependence of the critical current (Fig. 6). At zero field I_C varies smoothly with V_G (panel a), leading to a nearly constant $I_C R_N$ product away from the Dirac point. Upon increasing H_{\parallel} , I_C fluctuates with V_G (panels b-d) leading at $H_{\parallel} = 3$ T to patterns of decay and revival of $I_C(V_G)$. Observing the evolution of the interference pattern with V_G at the same field reveals a qualitative change in the number of visible lobes and in their positions (panel (e)).

The observed gate dependence of the interference pattern shows that at H_{\parallel} around the suppression-recovery field of 2.8T, the junction enters a new regime where the critical current survives in patches at fluctuating gate values. Similar phenomenology has been observed in ballistic graphene JJs at high perpendicular field, and attributed to chaotic billiards due to cyclotron orbits reflecting from the graphene edge [53]. However the physics in our regime is different, since the junction is diffusive and $B_{\perp} \approx 0$. Within the Zeeman effect interpretation, it could be due to local gate driven fluctuations around the $0-\pi$ transition as in [16]. Alternatively, when ripples become important, changing gate could change the resulting interference pattern. There could also be a gate-dependent effect in the contact region between the graphene and NbSe₂. In any case, clearly the current flow distribution in this regime depends strongly on graphene Fermi energy. This could be linked to local charge conditions such as the disorder potential landscape, however, the lobe structure continues to evolve when the graphene is at high carrier densities, where disorder potential should be screened.

We conclude that the 2DJJ architecture allows the study of graphene Josephson junctions at high parallel magnetic fields, where supercurrent is sensitive to both the Zeeman effect and sub-nm graphene height variations. Junction currents evolve from a Fraunhofer-like to a SQUID-like interference pattern.

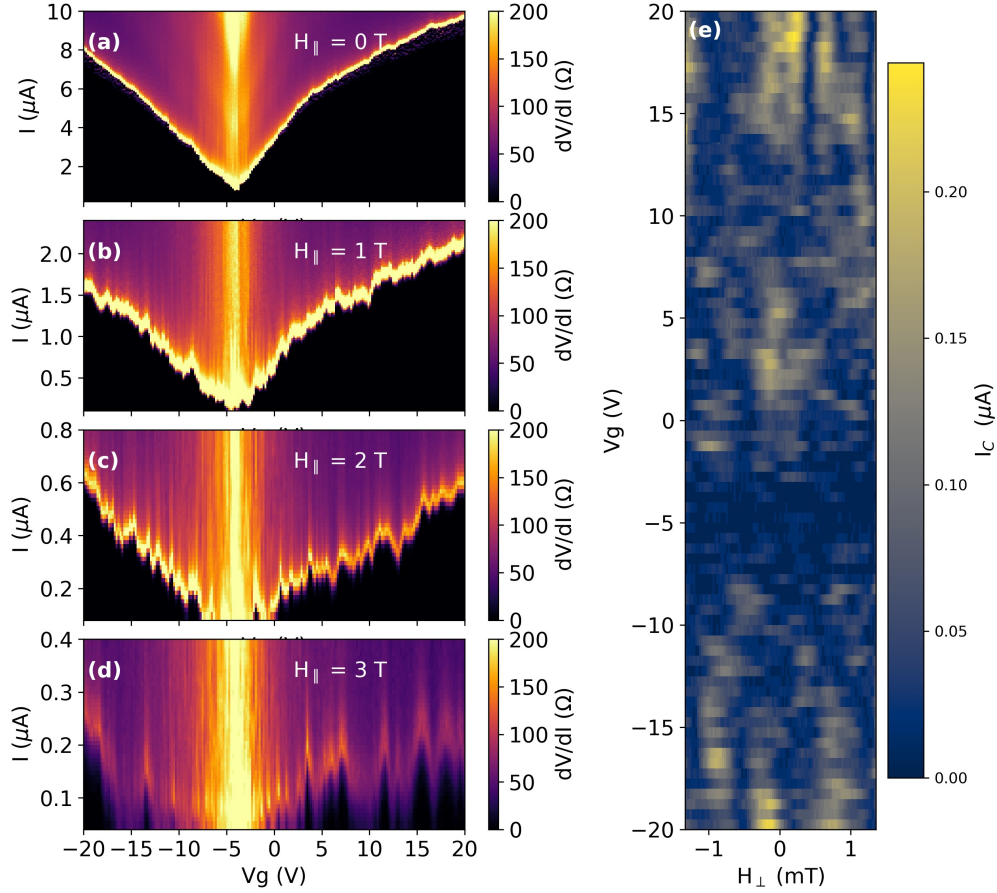


Figure 6: **a.-d.** Differential resistance of Junction A as a function of bias current and gate voltage, taken with applied in-plane magnetic field of 0, 1 T, 2 T, and 3 T respectively. All measurements conducted with $H_{\perp} = 0$. **e.** I_C vs. H_{\perp} and V_G for Junction A, taken with parallel field $H_{||} = 3$ T.

We observe a supercurrent suppression and recovery feature which may be associated with a Zeeman driven $0 - \pi$ transition, or with the accumulation of a single flux quantum within a μm -wavelength ripple. While in the present measurements it is difficult to distinguish between the two effects, future experiments, with graphene placed on hBN, are expected to suppress the ripple contribution. In the future it will be interesting to consider devices of the 2DJJ architecture utilizing different 2D materials as contacts and weak links. For example, devices where graphene inherits a spin-orbit term from a TMD substrate. The combination of significant spin-orbit and high parallel magnetic fields in the context of a Josephson junction, could give rise to topological effects [54].

The authors wish to thank M. Aprili, Y. Oreg, A. Stern, F. Pientka, and A. Di Bernardo for illuminating discussions. This work was funded by a European Research Council Starting Grant (No. 637298, TUNNEL), Israeli Science Foundation grant 861/19, and BSF grant 2016320. T.D. and A.Z.

are grateful to the Azrieli Foundation for Azrieli Fellowships. K.W. and T.T. acknowledge support from the Elemental Strategy Initiative conducted by the MEXT, Japan ,Grant Number JPMXP0112101001, JSPS KAKENHI Grant Number JP20H00354 and the CREST(JPMJCR15F3), JST.

1 Supplementary Section: Measurement and field alignment procedure

The system studied here, an SNS junction using graphene as the weak link between NbSe₂ SC leads, is very sensitive to the presence of perpendicular fields on the scale of hundreds of μT . When applying parallel magnetic field, perpendicular field can also be present, either from a small misalignment of the sample within the magnet, or from the presence of vortices and trapped magnetic flux in the leads, in the junction or in the magnet itself. At low parallel magnetic fields, the interference pattern of the supercurrent with the application of perpendicular field shows a clear maximum at zero applied field. Thus, it is possible to track the shift of this maximum with applied parallel field and find the sample misalignment. In the measurements reported in this work we have done so, and found the required amount of perpendicular field to compensate for this effect. The interference patterns reported here are always with respect to the corrected zero perpendicular field.

At higher magnetic fields, this correction is not enough, as remnant field, coming from vortices in the leads and trapped flux in the magnet affects the sample. To correct for that, we assume that a small change in the parallel field should not create a large change in the interference pattern of the junction. Based on this assumption, when analyzing the data, we use the following alignment procedure: We shift the interference pattern measured at a given parallel field by a some amount of perpendicular field. We calculate the sum of the squared differences between an this pattern and the pattern measured in the previous parallel field. We repeat this for a series of shifts and find for which shift this difference is minimal. We choose this shift as the correct alignment for the pattern, and repeat with the pattern taken at the next step of the parallel field.

The above procedure was utilized for junction A. For other junctions, we could not determine the orientation of $H_{\perp}=0\text{T}$ at high values of H_{\parallel} due to jumps in the interference pattern. Therefore we used the maximal critical current I_C^{max} as an indicator of the junction critical current.

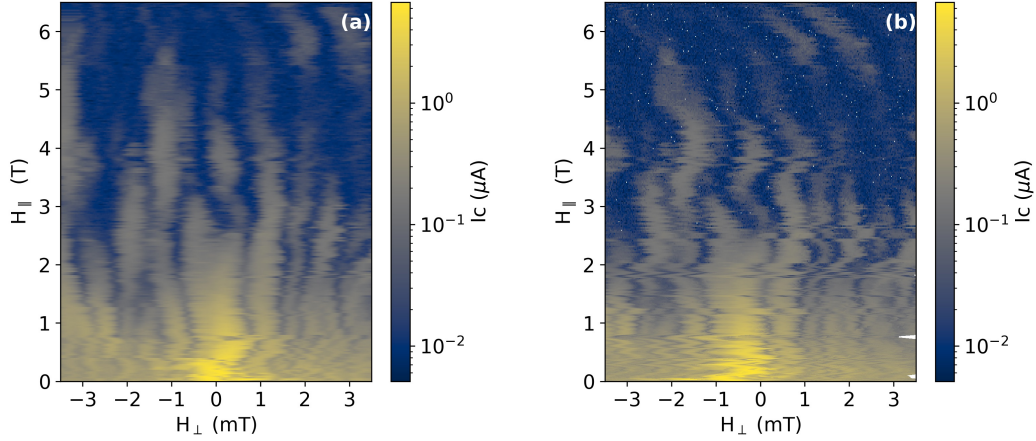


Figure 7: (a) The 2D map of I_C of Junction A as a function of H_{\parallel} and H_{\perp} , aligned using the full alignment procedure of minimizing the squared difference between line-scans and shown also in main text Fig. 2(f). (b) The same data shown when only geometrical misalignment was taken into consideration.

2 Supplementary Section: Simulation of ripples in graphene

We assume the presence of height variations in graphene, and in the absence of the Zeeman effect (taking $E_{Th} \gg E_Z$), theoretically calculate the critical current expected for Junction A, shown in main text Fig. 3 panel (b). We calculated this for eight different ripple profiles, generated by taking a sum of a random number of sine functions, all with randomized wavelength, amplitude and angular offsets. The wavelengths were taken from an exponential distribution (meaning that longer wavelengths are more probable) while the rest of the parameters were taken from uniform distributions. Qualitative features such as a transition in the lobe structure from Fraunhofer-like to SQUID-like, decay of the critical current and a suppression and reappearance of $I_C(H_{\perp}=0)$ appear for several of the randomly generated profiles. The specific result we chose to present in the main text was generated from the following ripple profile:

$$\eta(x, y) = 1.25 \sin 64.6y + 1.7164 \sin 3.5x - 0.7 + 0.45 \sin 37.3y + 2.136 \sin 2x + 1.3 \sin 2y + 0.3224 \sin 0.1x + 0.03 \quad (5)$$

Ripple amplitude is given in nm, while the coordinates x, y are normalized and range between -0.5, 0.5. The profiles were chosen with wavelengths much larger than 50 nm, in order to accommodate the use of the wide-junction approximation [55]. The junction length profile used for the combined simulation of Zeeman, ripple and junction geometry effects presented in main text Fig. 3 panel (c), is illustrated in Fig. 8.

3 Supplementary Section: Additional junctions

We present critical current measurements from devices B, C, D, showing I_C vs H_{\perp} (Junction B has a weak link of bilayer graphene, the rest are monolayer). This exhibits a Fraunhofer-like interference at

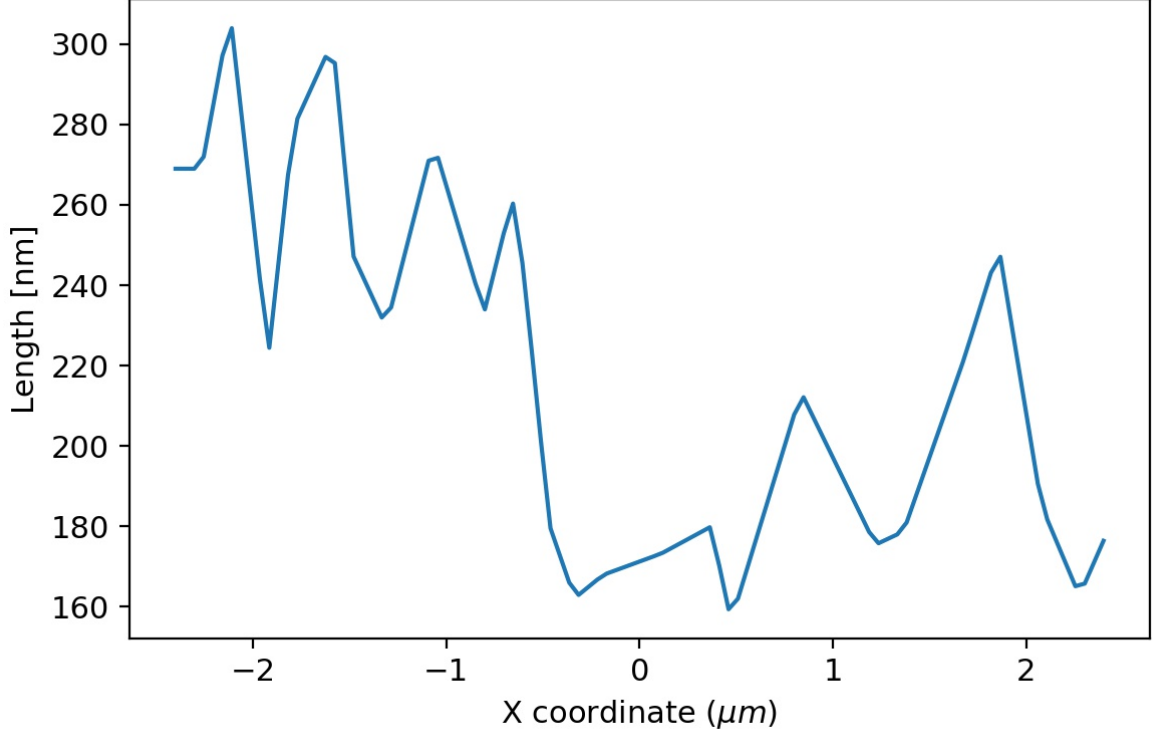


Figure 8: The junction length profile of Junction A as measured by SEM.

low H_{\parallel} and a more SQUID-like lobe structure, with lobes having a similar maximal I_C , at higher H_{\parallel} for each device. Junction D has a nonuniform geometry with multiple graphene weak links, making it difficult to directly interpret the interference pattern. Roughly, the lobe structure at $H_{\parallel}=0$ has a large area non-uniform component leading to high frequency lobes, modulated by a slow decay due to the uniform current in an individual small junction. The later modulation becomes more uniform as H_{\parallel} increases, as in the other devices.

4 Supplementary Section: Fabrication Methods

To fabricate a graphene - NbSe₂ Josephson junction (JJ), we first exfoliate graphene on marked SiO₂ and locate suitable flakes. Next, NbSe₂ is exfoliated on PDMS gel and examined to find flakes which are a few layers thick and have an observable crack, less than 500 nm wide. Chosen NbSe₂ flakes are transferred onto graphene using the viscoelastic dry-transfer method [56]. A few nm thick hBN flake may then be transferred over the crack to serve as a protective layer and a potential top-gate dielectric. The NbSe₂ flake is contacted with standard e-beam lithography using Ti/Au contacts. Prior to evaporation of contacts surface oxide was removed using Argon ion milling. Four-probe measurements were conducted in a dilution cryostat with a base temperature of 30 mK (see main text Fig. 1).

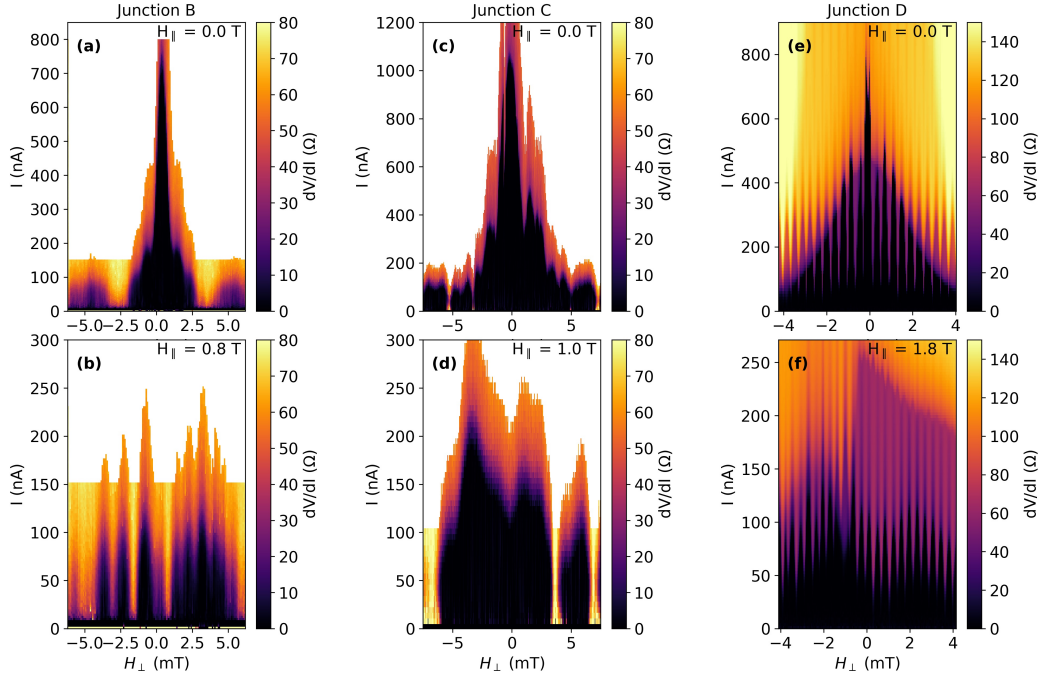


Figure 9: **Interference patterns from Junctions B,C,D** (a-c) Interference patterns of Junctions B,C,D respectively at $H_{\parallel}=0$ T showing a pronounced central lobe in each case (d-e) Interference patterns at various values of non-zero H_{\parallel} (indicated in the panel) for device B,D,C respectively. These patterns have all lobes with similar maximal values of I_C , indicating a non-uniform current distribution

References

- [1] D. K. Efetov, L. Wang, C. Handschin, K. B. Efetov, J. Shuang, R. Cava, T. Taniguchi, K. Watanabe, J. Hone, C. R. Dean, and P. Kim. Specular interband Andreev reflections at van der Waals interfaces between graphene and NbSe₂. Nat. Phys. 12, 328 (2016).
- [2] M. R. Sahu, X. Liu, A. K. Paul, S. Das, P. Raychaudhuri, J. K. Jain, and A. Das. Inter-Landau-level Andreev Reflection at the Dirac Point in a Graphene Quantum Hall State Coupled to a NbSe₂ Superconductor. Phys. Rev. Lett. 121, 086809 (2018).
- [3] J. Lee, M. Kim, K. Watanabe, T. Taniguchi, G. H. Lee, and H. J. Lee. Planar graphene Josephson coupling via van der Waals superconducting contacts. Curr. Appl. Phys. 19, 251 (2019).
- [4] X. Xi, Z. Wang, W. Zhao, J. H. Park, K. T. Law, H. Berger, L. Forró, J. Shan, and K.F. Mak. Ising pairing in superconducting NbSe₂ atomic layers. Nat. Phys. 12, 139 (2016).
- [5] T. Dvir, F. Massee, L. Attias, M. Khodas, M. Aprili, C. H. L. Quay, and H. Steinberg. Spectroscopy of bulk and few-layer superconducting NbSe₂ with van der Waals tunnel junctions. Nat. Comm. 9, 598 (2018).

- [6] T. Dvir, M. Aprili, C. H. L. Quay, and H. Steinberg. Zeeman Tunability of Andreev Bound States in van der Waals Tunnel Barriers. *Phys. Rev. Lett.* 123, 217003 (2019).
- [7] J. Linder, T. Yokoyama, D. Huertas-Hernando, and A. Sudbø. Supercurrent switch in graphene π junctions. *Phys. Rev. Lett.* 100, 187004 (2008).
- [8] Q. Liang, Y. Yu, Q. Wang, and J. Dong. Controllable $0-\pi$ Transition in a Superconducting Graphene-Nanoribbon Junction. *Phys. Rev. Lett.* 101, 187002 (2008).
- [9] A. G. Moghaddam and M. Zareyan. Long-range Josephson coupling through ferromagnetic graphene. *Phys. Rev. B* 78, 115413 (2008).
- [10] Y. Asano, T. Yoshida, Y. Tanaka, and A. A. Golubov. Electron transport in a ferromagnet-superconductor junction on graphene. *Phys. Rev. B* 78, 014514 (2008).
- [11] H. J. Suominen, J. Danon, M. Kjaergaard, K. Flensberg, J. Shabani, C. J. Palmstrøm, F. Nichele, and C. M. Marcus. Anomalous Fraunhofer interference in epitaxial superconductor-semiconductor Josephson junctions. *Phys. Rev. B* 95, 035307 (2017).
- [12] P. Fulde and R. A. Ferrell. Superconductivity in a Strong Spin-Exchange Field. *Phys. Rev.* 135, A550 (1964).
- [13] A. I. Larkin and Y. N. Ovchinnikov. Inhomogeneous state of superconductors. *Sov. Phys. JETP* 20, 762 (1965).
- [14] A. Q. Chen, M. J. Park, S. T. Gill, Y. Xiao, D. R. Plessis, G. J. MacDougall, M. J. Gilbert, and N. Mason. Finite momentum Cooper pairing in three-dimensional topological insulator Josephson junctions. *Nat. Comm.* 9, 3478 (2018).
- [15] S. Hart, H. Ren, M. Kosowsky, G. Ben-Shach, P. Leubner, C. Brüne, H. Buhmann, L. W. Molenkamp, B. I. Halperin, and A. Yacoby. Controlled finite momentum pairing and spatially varying order parameter in proximitized HgTe quantum wells. *Nat. Phys.* 13, 87 (2016).
- [16] C. T. Ke, C. M. Moehle, F. K. Vries, C. Thomas, S. Metti, C. R. Guinn, R. Kallaher, M. Lodari, G. Scappucci, T. Wang, R. E. Diaz, G. C. Gardner, M. J. Manfra, and S. Goswami. Ballistic Superconductivity and Tunable π Junctions in InSb Quantum Wells. *Nat. Comm.* 10, 3764 (2019).
- [17] C. Li, B. de Ronde, J. de Boer, J. Ridderbos, F. Zwanenburg, Y. Huang, A. Golubov, and A. Brinkman. Zeeman-Effect-Induced $0-\pi$ Transitions in Ballistic Dirac Semimetal Josephson Junctions. *Phys. Rev. Lett.* 123, 026802 (2019).
- [18] J. Linder, A. M. Black-Schaffer, and A. Sudbø. Triplet proximity effect and odd-frequency pairing in graphene. *Phys. Rev. B* 82, 041409 (2010).
- [19] E. H. Fyhn, M. Amundsen, A. Zalic, T. Dvir, H. Steinberg, and J. Linder. Combined Zeeman and orbital effect on the Josephson effect in rippled graphene. *Phys. Rev. B* 102, 024510 (2020).

- [20] See Supplemental Material at [URL will be inserted by publisher] for magnetic field alignment procedure (Section 1), information on simulation of ripples in graphene (Section 2), measurements from additional samples (Section 3), and fabrication methods (Section 4).
- [21] H. B. Heersche, P. Jarillo-Herrero, J. B. Oostinga, L. M. K. Vandersypen, and A. F. Morpurgo. Bipolar supercurrent in graphene. *Nature* 446, 56 (2007).
- [22] D. Jeong, J. H. Choi, G. H. Lee, S. Jo, Y. J. Doh, and H. J. Lee. Observation of supercurrent in PbIn-graphene-PbIn Josephson junction. *Phys. Rev. B* 83, 094503 (2011).
- [23] K. Komatsu, C. Li, S. Autier-Laurent, H. Bouchiat, and S. Guéron. Superconducting proximity effect in long superconductor/graphene/superconductor junctions: From specular Andreev reflection at zero field to the quantum Hall regime. *Phys. Rev. B* 86, 115412 (2012).
- [24] C. T. Ke, I. V. Borzenets, A. W. Draelos, F. Amet, Y. Bomze, G. Jones, M. Craciun, S. Russo, M. Yamamoto, S. Tarucha, and G. Finkelstein. Critical Current Scaling in Long Diffusive Graphene-Based Josephson Junctions. *Nano Lett.* 16, 4788 (2016).
- [25] C. Li, S. Guéron, A. Chepelianskii, and H. Bouchiat. Full range of proximity effect probed with superconductor/graphene/superconductor junctions. *Phys. Rev. B* 94, 115405 (2016).
- [26] J. C. Hammer, J. C. Cuevas, F. S. Bergeret, W. Belzig. Density of states and supercurrent in diffusive SNS junctions: Roles of nonideal interfaces and spin-flip scattering. *Phys. Rev. B* 76, 064514 (2007).
- [27] A. N. Tahvildar-Zadeh, J. K. Freericks, and B. K. Nikolić. Thouless energy as a unifying concept for Josephson junctions tuned through the Mott metal-insulator transition. *Phys. Rev. B* 73, 184515 (2006).
- [28] E. Khestanova, J. Birkbeck, M. Zhu, Y. Cao, G. L. Yu, D. Ghazaryan, J. Yin, H. Berger, L. Forró, T. Taniguchi, K. Watanabe, R. V. Gorbachev, A. Mishchenko, A. K. Geim and I. V. Grigorieva. Unusual Suppression of the Superconducting Energy Gap and Critical Temperature in Atomically Thin NbSe₂ *Nano Lett.* 18, 2623 (2018).
- [29] P. Dubos, H. Courtois, B. Pannetier, FK Wilhelm, AD Zaikin, and G. Schön. Josephson critical current in a long mesoscopic SNS junction. *Phys. Rev. B* 63, 064502 (2001).
- [30] F. D. Callaghan, M. Laulajainen, C. V. Kaiser, and J. E. Sonier. Field dependence of the vortex core size in a multiband superconductor. *Phys. Rev. Lett.* 95, 197001 (2005).
- [31] E. F. Talantsev, W. P. Crump, J. O. Island, Y. Xing, Y. Sun, J. Wang, and J. L. Tallon. On the origin of critical temperature enhancement in atomically thin superconductors. *2D Mat.* 4, 025072 (2017).
- [32] M. T. Allen, O. Shtanko, I. C. Fulga, A. R. Akhmerov, K. Watanabe, T. Taniguchi, P. Jarillo-Herrero, L. S. Levitov, and A. Yacoby. Spatially resolved edge currents and guided-wave electronic states in graphene. *Nat. Phys.* 12, 128 (2016).

- [33] M. J. Zhu, A. V. Kretinin, M. D. Thompson, D. A. Bandurin, S. Hu, G. L. Yu, J. Birkbeck, A. Mishchenko, I. J. Vera-Marun, K. Watanabe, T. Taniguchi, M. Polini, J. R. Prance, K. S. Novoselov, A. K. Geim, and M. Ben Shalom. Edge currents shunt the insulating bulk in gapped graphene. *Nat. Comm.* 8, 6 (2017).
- [34] A. Rasmussen, J. Danon, H. Suominen, F. Nichele, M. Kjaergaard, and K. Flensberg. Effects of spin-orbit coupling and spatial symmetries on the Josephson current in SNS junctions. *Phys. Rev. B* 93, 155406 (2016).
- [35] A. Assouline, C. Feuillet-Palma, N. Bergeal, T. Zhang, A. Mottaghizadeh, A. Zimmers, E. Lhuillier, M. Eddrie, P. Atkinson, M. Aprili, and H. Aubin. Spin-Orbit induced phase-shift in Bi_2Se_3 Josephson junctions. *Nat. Comm.* 10, 126 (2019).
- [36] T. Golod, A. Rydh, and V. M. Krasnov. Detection of the phase shift from a single Abrikosov vortex. *Phys. Rev. Lett.* 104, 227003 (2010).
- [37] V. M. Krasnov. Josephson junctions in a local inhomogeneous magnetic field. *Phys. Rev. B* 101, 144507 (2020).
- [38] T. Kontos, M. Aprili, J. Lesueur, F. Genêt, B. Stephanidis, and R. Boursier. Josephson Junction through a Thin Ferromagnetic Layer: Negative Coupling. *Phys. Rev. Lett.* 89, 137007 (2002).
- [39] W. Guichard, M. Aprili, O. Bourgeois, T. Kontos, J. Lesueur, and P. Gandit. Phase Sensitive Experiments in Ferromagnetic-Based Josephson Junctions. *Phys. Rev. Lett.* 90, 167001 (2003).
- [40] Y. Blum, A. Tsukernik, M. Karpovski, and A. Palevski. Oscillations of the Superconducting Critical Current in Nb-Cu-Ni-Cu-Nb Junctions. *Phys. Rev. Lett.* 89, 187004 (2002).
- [41] V. A. Oboznov, V. V. Bol'ginov, A. K. Feofanov, V. V. Ryazanov, and A. I. Buzdin. Thickness Dependence of the Josephson Ground States of Superconductor-Ferromagnet-Superconductor Junctions. *Phys. Rev. Lett.* 96, 197003 (2006).
- [42] V. Shelukhin, A. Tsukernik, M. Karpovski, Y. Blum, K. B. Efetov, A. F. Volkov, T. Champel, M. Eschrig, T. Löfwander, G. Schon, and A. Palevski. Observation of periodic π -phase shifts in ferromagnet-superconductor multilayers. *Phys. Rev. B* 73, 174506 (2006).
- [43] J. W. A. Robinson, S. Piano, G. Burnell, C. Bell, and M. G. Blamire. Critical Current Oscillations in Strong Ferromagnetic π Junctions. *Phys. Rev. Lett.* 97, 177003 (2006).
- [44] A. I. Buzdin. Proximity effects in superconductor-ferromagnet heterostructures. *Rev. Mod. Phys.* 77, 935 (2005).
- [45] M. Kemmler, M. Weides, M. Weiler, M. Opel, S. T. B. Goennenwein, A. S. Vasenko, A. A. Golubov, H. Kohlstedt, D. Koelle, R. Kleiner, and E. Goldobin. Magnetic interference patterns in $0-\pi$ superconductor/insulator/ferromagnet/superconductor josephson junctions: Effects of asymmetry between 0 and π regions. *Phys. Rev. B* 81, 054522 (2010).

- [46] S. M. Frolov, D. J. Van Harlingen, V. V. Bolginov, V. A. Oboznov, and V. V. Ryazanov. Josephson interferometry and Shapiro step measurements of superconductor-ferromagnet-superconductor $0-\pi$ junctions. *Phys. Rev. B* 74, 020503 (2006).
- [47] J. Pfeiffer, M. Kemmler, D. Koelle, R. Kleiner, E. Goldobin, M. Weides, A. K. Feofanov, J. Lisenfeld, and A. V. Ustinov. Static and dynamic properties of 0 , π , and $0-\pi$ ferromagnetic Josephson tunnel junctions. *Phys. Rev. B* 77, 214506 (2008).
- [48] M. Weides, M. Kemmler, H. Kohlstedt, R. Waser, D. Koelle, R. Kleiner, and E. Goldobin. $0-\pi$ Josephson tunnel junctions with ferromagnetic barrier. *Phys. Rev. Lett.* 97, 247001 (2006).
- [49] M. Ishigami, J. H. Chen, W. G. Cullen, M. S. Fuhrer, and E. D. Williams. Atomic structure of graphene on SiO_2 . *Nano Lett.* 7, 1643 (2007).
- [50] V. Geringer, M. Liebmann, T. Echtermeyer, S. Runte, M. Schmidt, R. Rückamp, M. C. Lemme, and M. Morgenstern. Intrinsic and extrinsic corrugation of monolayer graphene deposited on SiO_2 . *Phys. Rev. Lett.* 102, 076102 (2009).
- [51] W. G. Cullen, M. Yamamoto, K. M. Burson, J. H. Chen, C. Jang, L. Li, M. S. Fuhrer, and E. D. Williams. High-fidelity conformation of graphene to SiO_2 topographic features. *Phys. Rev. Lett.* 105, 215504 (2010).
- [52] J. Xue, J. Sanchez-Yamagishi, D. Bulmash, P. Jacquod, A. Deshpande, K. Watanabe, T. Taniguchi, P. Jarillo-Herrero, and B. J. LeRoy. Scanning tunnelling microscopy and spectroscopy of ultra-flat graphene on hexagonal boron nitride. *Nat. Mat.* 10, 282 (2011).
- [53] M. B. Shalom, M. J. Zhu, V. I. Fal, A. Mishchenko, A. V. Kretinin, K. S. Novoselov, C. R. Woods, K. Watanabe, T. Taniguchi, A. K. Geim and J. R. Prance. Quantum oscillations of the critical current and high-field superconducting proximity in ballistic graphene *Nat. Phys.* 12, 318 (2016).
- [54] T. Wakamura, N. J. Wu, A. D. Chepelianskii, S. Guéron, M. Och, M. Ferrier, T. Taniguchi, K. Watanabe, C. Mattevi, and H. Bouchiat. Spin-orbit-enhanced robustness of supercurrent in graphene/ WS_2 Josephson junctions. *Phys. Rev. Lett.* 125, 266801 (2020).
- [55] F. S. Bergeret and J. C. Cuevas. The vortex state and Josephson critical current of a diffusive SNS junction. *J. Low. Temp. Phys.* 153, 304 (2008).
- [56] A. Castellanos-Gomez, M. Buscema, R. Molenaar, V. Singh, L. Janssen, H. S. J. van der Zant, and G. A. Steele. Deterministic transfer of two-dimensional materials by all-dry viscoelastic stamping. *2D Mat.* 1, 011002 (2014).